

Lead-free halide double perovskite-polymer
composites for flexible X-ray imaging†Cite this: *J. Mater. Chem. C*, 2018,
6, 11961Received 4th April 2018,
Accepted 6th August 2018

DOI: 10.1039/c8tc01564c

rsc.li/materials-c

Haoran Li,^a Xin Shan,^a Jennifer N. Neu,^{bc} Thomas Geske,^d Melissa Davis,^a
Pengsu Mao,^a Kai Xiao,^e Theo Siegrist^{bcd} and Zhibin Yu^{id}*^{ad}

X-ray detectors are demonstrated using composite films of lead-free Cs₂AgBiBr₆ halide double perovskite embedded in a polymer matrix as the X-ray photoconductors. Polymers with hydroxyl functional groups greatly improve the uniformity of the composite films, and large area dense films are obtained using a simple drop-casting process. X-ray detectors based on the composite films exhibit a sensitivity of 40 μC Gy_{air}⁻¹ cm⁻², comparable to the reported sensitivity using Cs₂AgBiBr₆ single crystals. Such detectors can also tolerate a 5% tensile/compressive strain in the composite films without performance degradation. Pixelated X-ray detectors fabricated on the same composite film can realize X-ray imaging and resolve a proof-of-concept geometric pattern.

1. Introduction

Digital X-ray imaging finds important applications for medical diagnostics, security screening, and industrial product inspection. Two imaging mechanisms are commonly adopted that involve absorbing the incoming X-ray photons and converting them to mobile charge carriers using photoconductors or lower energy photons with scintillation phosphors.¹ Photoconductors normally exceed phosphors in spatial resolution which is beneficial for the identification of small objects and fine features.² Thus far, amorphous selenium,³ polycrystalline cadmium telluride⁴ and crystalline silicon⁵ based materials have been mostly investigated as X-ray photoconductors. The requirements of high

vacuum and/or high temperature processes for these materials have limited their potential for low-cost large area applications.

Recently, a group of halide perovskite semiconductors have attracted a lot of attention due to their superior charge transport properties and their solubility in certain organic solvents.^{6–8} Solution-processed solar cells and light-emitting diodes (LEDs) with very high efficiencies have been demonstrated.^{9–15} At the same time, many halide perovskite compounds consist of elements with large atomic numbers that are essential for obtaining a high stopping power for high energy photons, spurring an interest of applying these compounds for X-ray and gamma-ray detection.^{16–27} For instance, both Yakunin *et al.*¹⁶ and Kim *et al.*¹⁷ used solution-processed methylammonium lead triiodide (MAPbI₃) films for X-ray detection. Shrestha *et al.*¹⁸ developed wafer-scale MAPbI₃ films using a room-temperature sintering process. X-ray sensitivities of about 2.5 × 10³ to 2.5 × 10⁴ μC Gy_{air}⁻¹ cm⁻² in these perovskite-based detectors were demonstrated. Wei H. T. *et al.*¹⁹ and Wei W. *et al.*²⁰ prepared methylammonium lead tribromide (MAPbBr₃) single crystals and MAPbBr₃-silicon integrated crystals and reported sensitivities of 80 μC Gy_{air}⁻¹ cm⁻² and 2.1 × 10⁴ μC Gy_{air}⁻¹ cm⁻², respectively. Noticeably, the highest sensitivity has far exceeded those of commercial X-ray detectors based on amorphous selenium. In addition, Pan *et al.*²¹ worked on halide double perovskite (Cs₂AgBiBr₆) single crystals and obtained an X-ray sensitivity of 105 μC Gy_{air}⁻¹ cm⁻², signifying important steps towards solution-processed lead-free X-ray detectors. A summary of the above reported X-ray sensitivities is shown in Table S1 (ESI†). Nonetheless, mechanical flexibility was not considered in all previous reports.

Flexible X-ray detectors are of interest for their lightweight and ability to conformally adhere to uneven surfaces, enabling portable X-ray diagnostic tools and potentially reducing image distortion in cone beam computed tomography.²⁸ It is worth mentioning that flexible solar cells and LEDs have been achieved using thin layers (tens of nanometers to a few micrometers) of halide perovskites as the light absorbers or emitters.^{29–31} However, tens-of-micrometer thick halide perovskite layers are required to effectively absorb X-rays,¹⁷ but films with

^a Department of Industrial and Manufacturing Engineering, High-Performance Materials Institute, FAMU-FSU College of Engineering, Florida State University, Tallahassee, FL 32310, USA. E-mail: zyu@fsu.edu

^b Department of Chemical and Biomedical Engineering, FAMU-FSU College of Engineering, Florida State University, Tallahassee, FL 32310, USA

^c National High Magnetic Field Laboratory, Tallahassee, Florida 32310, USA

^d Materials Science and Engineering, Florida State University, Tallahassee, FL 32306, USA

^e Center for Nanophase Materials Sciences, Oak Ridge National Laboratory, Oak Ridge, TN 37831, USA

† Electronic supplementary information (ESI) available. See DOI: 10.1039/c8tc01564c

such thickness tend to crack and delaminate from the substrate under strain.

In this work, composite films consisting of a lead-free halide double perovskite embedded in a polymer matrix are explored as a new strategy to overcome the flexibility limitations in thick halide perovskite films. As a proof of concept, the double perovskite $\text{Cs}_2\text{AgBiBr}_6$ is used due to its low toxicity. Here, one Ag^+ and one Bi^{3+} replace two Pb^{2+} sites in the unit cells of haloplumbate perovskites while maintaining the corner-sharing metal-halide octahedral network of perovskite crystals.^{32–34} Polymers with hydroxyl functional groups greatly improve the dispersity of $\text{Cs}_2\text{AgBiBr}_6$ in the composite films, and large area dense films are easily obtained *via* a solution-based process. X-ray detectors based on the composite films exhibit a sensitivity of $40 \mu\text{C Gy}_{\text{air}}^{-1} \text{cm}^{-2}$ which is comparable to the literature result of $\text{Cs}_2\text{AgBiBr}_6$ single crystals.²¹ No performance degradation is observed after flexing/bending the detectors at a 2 mm radius, corresponding to a maximum 5% tensile/compressive strain in the composite films.

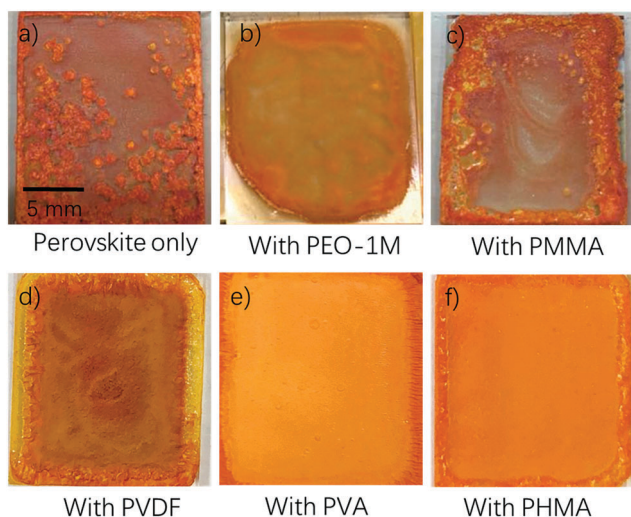


Fig. 1 Optical photos of solution-casted films on glass substrates. (a) Halide double perovskite ($\text{Cs}_2\text{AgBiBr}_6$) only, and $\text{Cs}_2\text{AgBiBr}_6$ -polymer composite films with (b) PEO ($M_w \sim 1\,000\,000$), (c) PMMA ($M_w \sim 120\,000$), (d) PVDF ($M_w \sim 530\,000$), (e) PVA ($M_w 89\,000\text{--}98\,000$), and (f) PHMA ($M_w \sim 300\,000$).

2. Experimental

2.1 Materials

Cesium bromide (CsBr , 99.9%), silver bromide (AgBr , 99%), bismuth(III) bromide (BiBr_3 , $\geq 98\%$), dimethyl sulfoxide (DMSO, anhydrous, 99.9%), poly(ethylene oxide) (PEO, average $M_w \sim 100\,000$, 600 000, and 1 000 000), poly(vinyl alcohol) (PVA, $M_w 89\,000\text{--}98\,000$, $>99\%$ hydrolyzed), poly(vinylidene fluoride) (PVDF, $M_w \sim 530\,000$), poly(methyl methacrylate) (PMMA, $M_w \sim 15\,000$, 120 000, and 350 000), and poly(2-hydroxyethyl methacrylate) (PHMA, $M_w \sim 300\,000$) were purchased from Sigma-Aldrich. All materials were used as received.

2.2 Film preparation and characterizations

The glass substrates were cleaned with detergent water, sonicated for 10 minutes each in acetone, IPA and distilled water and then blow dried with nitrogen. Cleaned glass substrates were treated with oxygen plasma at 100 W power for 3 minutes. CsBr , AgBr and BiBr_3 were mixed with 2:1:1 molar ratio and dissolved in DMSO with a concentration of 200 mg mL^{-1} . The polymers were also dissolved in DMSO and mixed with the perovskite precursor solution with 1:2 weight ratio (polymer/ $\text{Cs}_2\text{AgBiBr}_6$). The solution was then poured onto a cleaned glass substrate and dried inside a vacuum oven at 150°C for 12 hours. The dried film was peeled off from the glass substrate and used for material characterizations and X-ray detector fabrication. Field Emission SEM (JEOL-7401F), UV-Vis-NIR spectrometer (Varian Cary 5000), XRD (X'PERT Pro with $\text{Cu K}\alpha$ radiation source), and a fluorometer (Horiba JY Fluoromax-4) were used to characterize the composite thin films.

2.3 X-ray detector fabrication and measurement

Au contact electrodes were deposited in a vacuum thermal evaporator with a rate of 0.5 \AA s^{-1} under 10^{-6} Torr. Silver paste contact electrodes were fabricated *via* brushing PELCO[®] Conductive Silver Paint (16062) and allowed to dry for six hours at 60°C . Contact masks were used to define the electrode shape in thermal evaporation and screen printing. X-ray detection properties of the films were investigated using a standard fine-focus copper X-ray tube mounted in a Scintag PAD-V diffractometer, energized at 45 kV and 22.2 mA (1 kW electrical load).

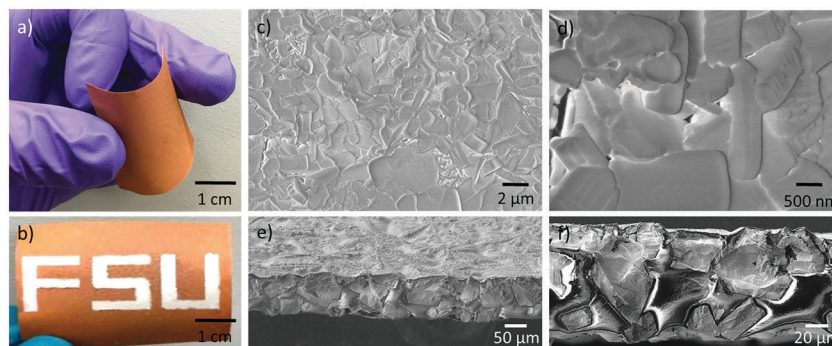


Fig. 2 Optical photos of (a) a $100 \mu\text{m}$ -thick $\text{Cs}_2\text{AgBiBr}_6/\text{PVA}$ (2:1 weight ratio) and (b) the film with screen-printed conductive silver paste as electrical contacts to the film. SEM top (c and d) and cross-section (e and f) images of the $\text{Cs}_2\text{AgBiBr}_6/\text{PVA}$ composite film.

The spectrum of the tube consists of a white background with cut-off at 45 kV, and the spectral lines of Cu K_{α} and K_{β} , as well as tungsten L-lines. No filter was applied.

3. Results and discussion

The optical photos of the pristine perovskite and perovskite-polymer composite films are shown in Fig. 1 and Fig. S1 (ESI[†]). If no polymer was present, scattered $\text{Cs}_2\text{AgBiBr}_6$ crystals or aggregates grew and the resulting film was highly non-uniform (Fig. 1a). Polyethylene oxide (PEO), polymethylmethacrylate (PMMA), polyvinylidene difluoride (PVDF), and polyvinyl alcohol (PVA) were first tested for dispersing the $\text{Cs}_2\text{AgBiBr}_6$ crystals. All composite films have a perovskite:polymer weight ratio of 2:1. PVA produced the most uniform film. The results were further confirmed by optical microscopic images as shown in Fig. S2 (ESI[†]). We hypothesize that the polar and protic features of the hydroxyl groups in the PVA increase their interactions with the halide perovskites.³⁵ To verify this hypothesis, poly(2-hydroxyethyl methacrylate), PHMA, was also tested. Compared to PMMA, PHMA has a similar chemical structure except additional hydroxyl functional groups on the side chains. As shown in Fig. 1f, the composite film using PHMA showed a greatly improved uniformity over the PMMA polymer, confirming the important role of the hydroxyl groups in producing homogenous halide perovskite/polymer composite films. PEO polymers with different molecular weights were also used. It is observed the composite film became much more uniform when a lower molecular weight PEO was used (Fig. S1a and b, ESI[†]). It is explained that the PEO with a lower molecular weight exhibits a higher concentration of hydroxyl groups locating at both ends of each polymer chain. In comparison, PMMA polymers with different molecular weights all showed poor film uniformity (Fig. S1c and d, ESI[†]). Such a finding demonstrates that the resulting film morphology is mostly independent on the molecular weight of the polymer if no hydroxyl groups are incorporated.

Separation of the thick composite films from the substrate is easily achieved *via* peeling of the films off the substrate. An optical image of a 100 μm -thick, free-standing $\text{Cs}_2\text{AgBiBr}_6$ /PVA (2:1 weight ratio) composite film is shown in Fig. 2a. The film has been bent with about 1 cm radius of curvature, demonstrating its mechanical flexibility due to the incorporation of the PVA. The film also tolerates many volatile organic solvents including toluene, alcohol, and acetone. Thus, metallization of the film is easily carried out using commercial conductive silver paste directly to the film as shown in Fig. 2b. This property is highly advantageous for future scalable manufacturing of pixelated detector arrays for X-ray imaging.

The microscopic morphology of the composite film was characterized with scanning electron microscopy (SEM). The pristine perovskite film shows noncontinuous morphology (Fig. S3a, ESI[†]) which is consistent with the optical photo and microscopic image in Fig. 1a and Fig. S2a (ESI[†]), respectively. The composite film with 5:1 (weight ratio) perovskite:PVA showed improved continuity compared to the pristine perovskite film,

however it was still not fully continuous (Fig. S3b and c, ESI[†]). For our device fabrication, 2:1 weight ratio was then used, and their morphology are shown in Fig. 2c-f.

The top surface of the 2:1 composite film shows fused grains with dimensions from sub-micrometer to a few micrometers. The grains have greatly improved surface coverage compared with the pristine perovskite film, leaving only a small areal fraction of holes with sizes from sub-100 nm to 1 μm range. These holes do not extend through the film as shown by the cross-sectional SEM images (Fig. 2e and f). Remarkably much larger perovskite crystals from 20 to 100 μm are seen underneath the film surface, and a large portion of these crystals interconnect with each other from the bottom to the top surface, providing the necessary pathways for charge carrier mobility. The size difference of perovskite grains on the top

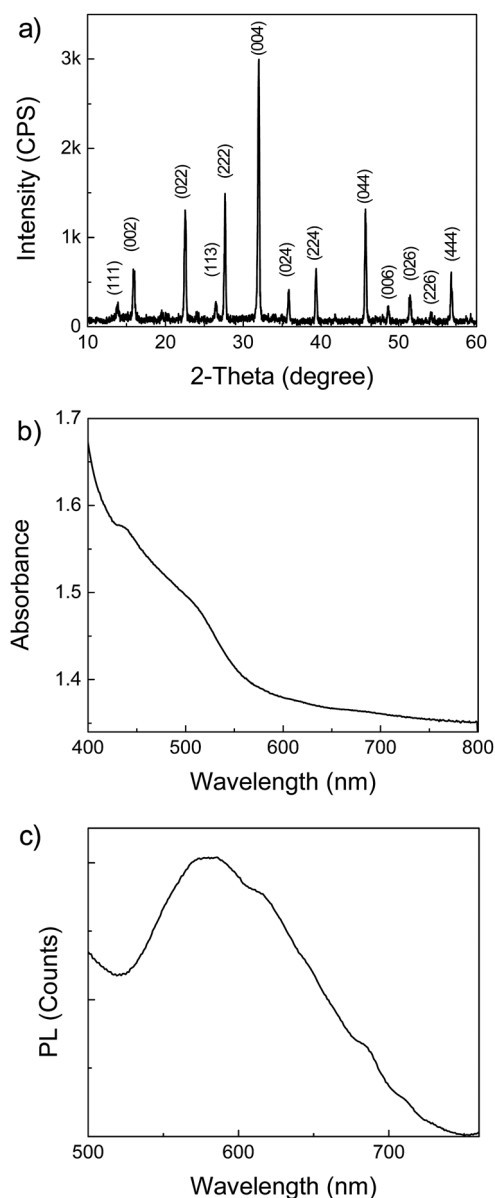


Fig. 3 (a) XRD pattern, (b) absorbance, and (c) PL spectrum of the $\text{Cs}_2\text{AgBiBr}_6$ /PVA (2:1 weight ratio) composite film.

surface and inside the film can be attributed to the solvent evaporation kinetics during film preparation. The top layer of the film dried first and formed a capping layer to reduce the solvent evaporation rate for the remaining solution, thus reducing nucleation densities and resulting in larger sized crystal precipitation inside the thick film.³⁶ Large grains are advantageous in polycrystalline semiconductor films due to reduced grain boundary defects, and the photo-excited charge carriers can be more efficiently collected in X-ray detectors.

The crystallinity of the composite film has been characterized by X-ray diffraction (XRD). As shown in Fig. 3a, the film shows the characteristic diffraction peaks of cubic phase $\text{Cs}_2\text{AgBiBr}_6$ with a lattice constant of 11.2 Å, which is in good agreement with

literature results.^{21,37} Fig. 3b and c show the absorbance and photoluminescence (PL) spectra of the composite film, respectively. The absorbance exhibits a gradual increase starting at around 600 nm towards shorter wavelengths, supporting an indirect electronic band gap of $\text{Cs}_2\text{AgBiBr}_6$ as reported by others.³⁷ The PL spectrum shows an emission peak at around 580 nm, corresponding to a band gap of about 2.1 eV for the $\text{Cs}_2\text{AgBiBr}_6$ crystals in the composite film. This value is also consistent with $\text{Cs}_2\text{AgBiBr}_6$ single crystals.²¹

We characterized the X-ray responses of the composite films, and devices were fabricated with a structure as shown in Fig. 4a. A vacuum evaporated gold (Au) thin film was used as the top contact, a free-standing $\text{Cs}_2\text{AgBiBr}_6/\text{PVA}$ composite film as the

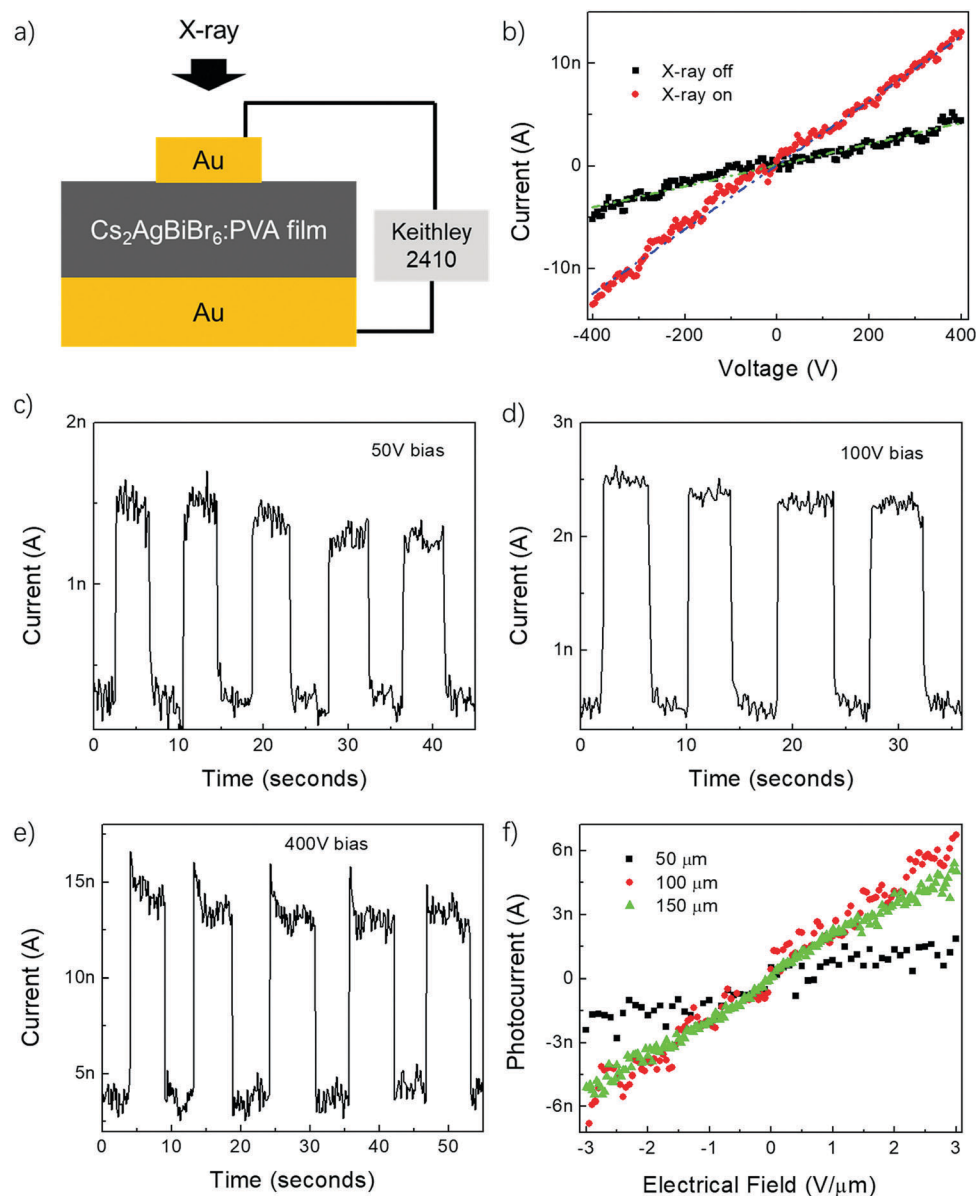


Fig. 4 (a) Schematically showing the device structure of X-ray detectors with the $\text{Cs}_2\text{AgBiBr}_6/\text{PVA}$ composite films as X-ray photoconductors. (b) The current–voltage (I – V) characteristics of a detector with a 100 μm -thick $\text{Cs}_2\text{AgBiBr}_6/\text{PVA}$ composite film at both X-ray on and off states. The dotted lines are linear fitting of the I – V curves. (c–e) Transient responses of the detector at a constant 50 V, 100 V, and 400 V, respectively. (f) Photocurrent–electrical field characteristics of X-ray detectors with 50 μm , 100 μm , and 150 μm -thick composite films.

X-ray absorber, and another layer of vacuum evaporated Au thin film as the bottom contact. X-ray irradiation was generated by a commercial X-ray copper tube (Scintag PAD-V diffractometer) at 45 kV and 22.2 mA (1 kW electrical load). The integrated emission intensity was calibrated as $13.8 \text{ mGy}_{\text{air}} \text{ s}^{-1}$ using a Geiger counter. Current–Voltage (I – V) characteristics were recorded with the X-ray beam in both on and off states. Fig. 4b shows the measurement results for a 2 mm^2 device fabricated from a $100 \mu\text{m}$ -thick composite film. Both the on and off curves are nearly linear within the tested voltage range, indicating ohmic electrical contacts between the composite film and the two Au electrodes. This result also suggests the $\text{Cs}_2\text{AgBiBr}_6$ –PVA composite film in this work is hole dominant (p-doped). From the approximate slopes of the curves, the incident X-ray flux has about tripled the charge carrier concentration in the composite film. The current on/off ratio remains at around three from -400 V to 400 V bias. This on/off ratio is believed to improve by adding an appropriate hole blocking layer at one of the electrode-composite film interfaces to reduce the off current.³⁸ Noticeably, the resistivity of the composite film when the X-ray is off is calculated to be about $2 \times 10^{11} \Omega \text{ cm}$. Such a high resistivity agrees well with a greatly reduced ionic mobility in the $\text{Cs}_2\text{AgBiBr}_6$ crystals compared to the haloplumbate perovskites.²¹

Transient responses of the X-ray detectors were also evaluated at a constant 50 V, 100 V, and 400 V as shown in Fig. 4c, d and e, respectively. In all cases, noticeable current increases were observed when the X-ray irradiation was turned on. As a control experiment, the device with a pure PVA polymer film had a

negligible response to X-ray on/off as shown in Fig. S4 (ESI[†]). At 400 V, the photocurrent reaches about 10 nA, leading to a sensitivity of $40 \mu\text{C Gy}_{\text{air}}^{-1} \text{ cm}^{-2}$. A comparable sensitivity has recently been reported using single crystalline $\text{Cs}_2\text{AgBiBr}_6$.²¹ Nonetheless, the use of composite films in this work has the advantage of manufacturing scalability capable to deliver large-area low-cost X-ray detectors.

Devices with different film thicknesses were also investigated, and a plot of photocurrent vs. applied electrical field is shown in Fig. 4f. Under the same electrical field, increasing film thickness from $50 \mu\text{m}$ to $100 \mu\text{m}$ has enhanced the photocurrent by about 100%. This result can be explained by an improved X-ray photon absorption and increased generation of mobile charge carriers in the thicker composite film. On the other hand, the $150 \mu\text{m}$ -thick film shows about the same photocurrent as the $100 \mu\text{m}$ film at the same applied electrical field bias, indicating the charge carrier collection has reached saturation in the $150 \mu\text{m}$ -thick film.

The flexibility of one X-ray detector based on a $100 \mu\text{m}$ composite film has been examined by measuring its current responses at a constant 100 V and with different bending radii. The device was conformally laminated onto the outer surface of a glass tube, as shown in Fig. 5a. The X-ray induced photocurrent increased from 1.6 nA in a flat device to 1.7 nA and 1.8 nA when the device was bent at 10 mm and 2 mm radii, respectively (Fig. 5b). The slight increase of the photocurrent may be due to an increase of exposure area in the bent device. These results imply that severe bending has not damaged the composite film,

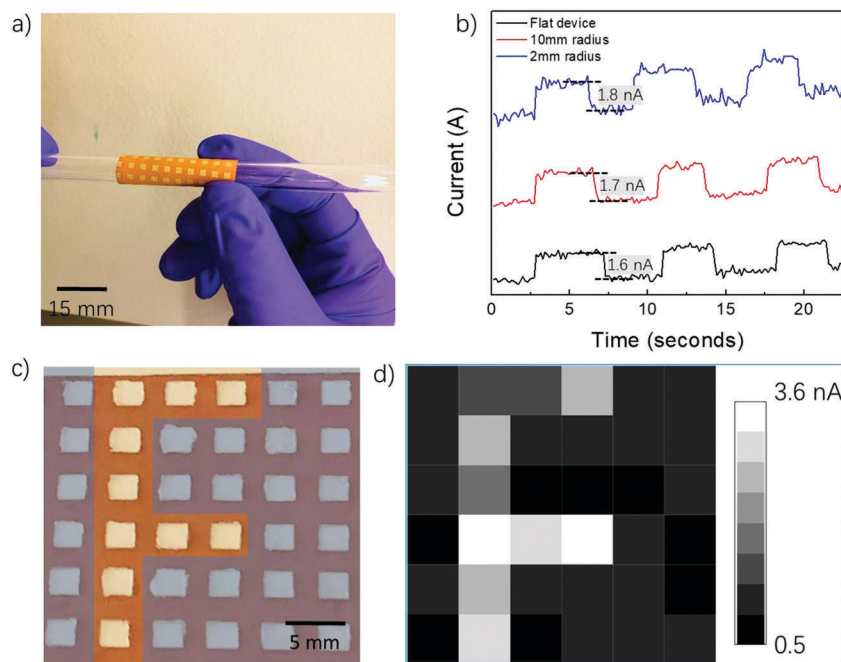


Fig. 5 (a) A photo showing an array of X-ray detectors fabricated on a $100 \mu\text{m}$ -thick $\text{Cs}_2\text{AgBiBr}_6$ /PVA composite film. The devices had 100 nm evaporated Au thin films as the top and bottom electrodes and the film was conformally wrapped around a 4 mm-diameter glass tube. (b) X-ray induced photocurrent responses of one detector at both flat and curved (10 mm and 2 mm bending radii) states. (c) A photo showing an X-ray imager with 6×6 detectors fabricated on a $100 \mu\text{m}$ -thick $\text{Cs}_2\text{AgBiBr}_6$ /PVA composite film. Silver paste islands were screen printed on the front side and a 100 nm-thick Au layer was evaporated on the back side of the film for electrical contacts. One $25 \mu\text{m}$ -thick molybdenum foil with an “F”-letter pattern was laminated on the Au film. (d) Photocurrent contrast among all the pixels resolved the “F” pattern of the molybdenum foil.

demonstrating its superior mechanical robustness for future flexible X-ray detector applications. It is also observed that the 100 nm gold film developed microcracks during bending test (Fig. S5, ESI†). Fortunately, the microcracks did not severely degrade the conductivity of the gold film (Fig. S6, ESI†), thus not affecting the flexibility performance evaluation of the composite film under X-ray irradiation. In the future, if more compliant contact electrodes are necessary, it is believed the gold can be replaced by carbon nanotubes or silver nanowires *etc.*^{39,40}

We continued our proof of concept by fabricating a pixelated X-ray imager with an array of 6×6 detector pixels on the same composite film (Fig. 5c). Silver paste was screen printed using a contact mask on one side of the thin film, and a 100 nm-thick Au layer was evaporated on the other side. The letter “F” was cut into a 25 μm -thick molybdenum foil and laminated onto the Au side of the X-ray imager. The imager was placed on a motorized stage, and the photocurrent of each detector pixel was recorded at a constant 100 V bias and the center of individual detector illuminated by the X-ray flux. A plot of the photocurrents for all the pixels is shown in Fig. 5d and has clearly resolved the pattern geometry of the molybdenum foil. A histogram of X-ray induced photocurrents is shown in Fig. S7 (ESI†) for the ten devices that were not covered by the molybdenum foil. We believe the scattering of photocurrents could be reduced by more processing optimizations to make more uniform composite films and sensing pixels.

4. Conclusion

We demonstrated X-ray detectors using composite films of lead-free $\text{Cs}_2\text{AgBiBr}_6$ halide double perovskite and a polymer as the X-ray photoconductors. Polymers containing hydroxyl functional groups were found most effective in dispersing the $\text{Cs}_2\text{AgBiBr}_6$ and obtaining uniform composite films with large embedded $\text{Cs}_2\text{AgBiBr}_6$ grains. X-ray detectors based on a free-standing 100 μm -thick composite film exhibited a sensitivity of $40 \mu\text{C Gy}_{\text{air}}^{-1} \text{cm}^{-2}$ at 400 V bias, and they could be bent with a 2 mm radius without degrading the photocurrent. The processing method and composite approach in this work can be potentially employed to other halide perovskite materials, for achieving solution-processed and flexible X-ray detectors and imagers with higher sensitivities.

Conflicts of interest

There are no conflicts to declare.

Acknowledgements

This work is financially supported by Air Force Office of Scientific Research under Award FA9550-16-1-0124. We thank Dr. Junqiang Li for technical assistance on the X-ray detection measurements. JN and TS acknowledge support by the National Science Foundation under grant NSF DMR 1606952. Part of the work was carried out at the National High Magnetic Field

Laboratory, which is supported by the National Science Foundation under grant NSF DMR 1644779, and the State of Florida. The portion of optical characterization was conducted at the Center for Nanophase Materials Sciences, which is a DOE Office of Science User Facility.

Notes and references

- 1 M. J. Yaffe and J. A. Rowlands, X-ray detectors for digital radiography, *Phys. Med. Biol.*, 1997, **42**(1), 1–39.
- 2 W. Que and J. A. Rowlands, X-Ray-Imaging Using Amorphous Selenium - Inherent Spatial-Resolution, *Med. Phys.*, 1995, **22**(4), 365–374.
- 3 W. Zhao and J. A. Rowlands, X-Ray-Imaging Using Amorphous Selenium - Feasibility of a Flat-Panel Self-Scanned Detector for Digital Radiology, *Med. Phys.*, 1995, **22**(10), 1595–1604.
- 4 T. Takahashi and S. Watanabe, Recent progress in CdTe and CdZnTe detectors, *IEEE Trans. Nucl. Sci.*, 2001, **48**(4), 950–959.
- 5 M. Jeong, W. J. Jo, H. S. Kim and J. H. Ha, Radiation hardness characteristics of Si-PIN radiation detectors, *Nucl. Instrum. Methods Phys. Res., Sect. A*, 2015, **784**, 119–123.
- 6 M. Gratzel, The light and shade of perovskite solar cells, *Nat. Mater.*, 2014, **13**(9), 838–842.
- 7 S. D. Stranks and H. J. Snaith, Metal-halide perovskites for photovoltaic and light-emitting devices, *Nat. Nanotechnol.*, 2015, **10**(5), 391–402.
- 8 C. Wehrenfennig, G. E. Eperon, M. B. Johnston, H. J. Snaith and L. M. Herz, High Charge Carrier Mobilities and Lifetimes in Organolead Trihalide Perovskites, *Adv. Mater.*, 2014, **26**(10), 1584–1589.
- 9 M. Z. Liu, M. B. Johnston and H. J. Snaith, Efficient planar heterojunction perovskite solar cells by vapour deposition, *Nature*, 2013, **501**(7467), 395.
- 10 N. J. Jeon, J. H. Noh, Y. C. Kim, W. S. Yang, S. Ryu and S. Il Seol, Solvent engineering for high-performance inorganic-organic hybrid perovskite solar cells, *Nat. Mater.*, 2014, **13**(9), 897–903.
- 11 N. J. Jeon, J. H. Noh, W. S. Yang, Y. C. Kim, S. Ryu, J. Seo and S. I. Seok, Compositional engineering of perovskite materials for high-performance solar cells, *Nature*, 2015, **517**(7535), 476.
- 12 M. Saliba, T. Matsui, J. Y. Seo, K. Domanski, J. P. Correa-Baena, M. K. Nazeeruddin, S. M. Zakeeruddin, W. Tress, A. Abate, A. Hagfeldt and M. Gratzel, Cesium-containing triple cation perovskite solar cells: improved stability, reproducibility and high efficiency, *Energy Environ. Sci.*, 2016, **9**(6), 1989–1997.
- 13 Z. K. Tan, R. S. Moggaddam, M. L. Lai, P. Docampo, R. Higler, F. Deschler, M. Price, A. Sadhanala, L. M. Pazos, D. Credgington, F. Hanusch, T. Bein, H. J. Snaith and R. H. Friend, Bright light-emitting diodes based on organometal halide perovskite, *Nat. Nanotechnol.*, 2014, **9**(9), 687–692.
- 14 H. C. Cho, S. H. Jeong, M. H. Park, Y. H. Kim, C. Wolf, C. L. Lee, J. H. Heo, A. Sadhanala, N. Myoung, S. Yoo, S. H. Im, R. H. Friend and T. W. Lee, Overcoming the electroluminescence efficiency

- limitations of perovskite light-emitting diodes, *Science*, 2015, **350**(6265), 1222–1225.
- 15 X. L. Yang, X. W. Zhang, J. X. Deng, Z. M. Chu, Q. Jiang, J. H. Meng, P. Y. Wang, L. Q. Zhang, Z. G. Yin and J. B. You, Efficient green light-emitting diodes based on quasi-two-dimensional composition and phase engineered perovskite with surface passivation, *Nat. Commun.*, 2018, **9**, 570.
 - 16 S. Yakunin, M. Sytnyk, D. Kriegner, S. Shrestha, M. Richter, G. J. Matt, H. Azimi, C. J. Brabec, J. Stangl, M. V. Kovalenko and W. Heiss, Detection of X-ray photons by solution-processed lead halide perovskites, *Nat. Photonics*, 2015, **9**(7), 444.
 - 17 Y. C. Kim, K. H. Kim, D. Y. Son, D. N. Jeong, J. Y. Seo, Y. S. Choi, I. T. Han, S. Y. Lee and N. G. Park, Printable organometallic perovskite enables large-area, low-dose X-ray imaging, *Nature*, 2017, **550**(7674), 87.
 - 18 S. Shrestha, R. Fischer, G. J. Matt, P. Feldner, T. Michel, A. Osvet, I. Levchuk, B. Merle, S. Golkar, H. W. Chen, S. F. Tedde, O. Schmidt, R. Hock, M. Ruhrig, M. Goken, W. Heiss, G. Anton and C. J. Brabec, High-performance direct conversion X-ray detectors based on sintered hybrid lead triiodide perovskite wafers, *Nat. Photonics*, 2017, **11**(7), 436.
 - 19 H. T. Wei, Y. J. Fang, P. Mulligan, W. Chuirazzi, H. H. Fang, C. C. Wang, B. R. Ecker, Y. L. Gao, M. A. Loi, L. Cao and J. S. Huang, Sensitive X-ray detectors made of methylammonium lead tribromide perovskite single crystals, *Nat. Photonics*, 2016, **10**(5), 333.
 - 20 W. Wei, Y. Zhang, Q. Xu, H. T. Wei, Y. J. Fang, Q. Wang, Y. H. Deng, T. Li, A. Gruverman, L. Cao and J. S. Huang, Monolithic integration of hybrid perovskite single crystals with heterogenous substrate for highly sensitive X-ray imaging, *Nat. Photonics*, 2017, **11**(5), 315.
 - 21 W. C. Pan, H. D. Wu, J. J. Luo, Z. Z. Deng, C. Ge, C. Chen, X. W. Jiang, W. J. Yin, G. D. Niu, L. J. Zhu, L. X. Yin, Y. Zhou, Q. G. Xie, X. X. Ke, M. L. Sui and J. Tang, Cs₂AgBiBr₆ single-crystal X-ray detectors with a low detection limit, *Nat. Photonics*, 2017, **11**(11), 726.
 - 22 S. Yakunin, D. N. Dirin, Y. Shynkarenko, V. Morad, I. Cherniukh, O. Nazarenko, D. Kreil, T. Nauser and M. V. Kovalenko, Detection of gamma photons using solution-grown single crystals of hybrid lead halide perovskites, *Nat. Photonics*, 2016, **10**(9), 585–589.
 - 23 D. N. Dirin, I. Cherniukh, S. Yakunin, Y. Shynkarenko and M. V. Kovalenko, Solution-Grown CsPbBr₃ Perovskite Single Crystals for Photon Detection, *Chem. Mater.*, 2016, **28**(23), 8470–8474.
 - 24 H. T. Wei, D. DeSantis, W. Wei, Y. H. Deng, D. Y. Guo, T. J. Savenije, L. Cao and J. S. Huang, Dopant compensation in alloyed CH₃NH₃PbBr₃ – xCl_x perovskite single crystals for gamma-ray spectroscopy, *Nat. Mater.*, 2017, **16**(8), 826.
 - 25 O. Nazarenko, S. Yakunin, V. Morad, I. Cherniukh and M. V. Kovalenko, Single crystals of caesium formamidinium lead halide perovskites: solution growth and gamma dosimetry, *NPG Asia Mater.*, 2017, **9**, e373.
 - 26 N. Kawano, M. Koshimizu, G. Okada, Y. Fujimoto, N. Kawaguchi, T. Yanagida and K. Asai, Scintillating Organic-Inorganic Layered Perovskite-type Compounds and the Gamma-ray Detection Capabilities, *Sci. Rep.*, 2017, **7**, 14754.
 - 27 M. D. Birowosuto, D. Cortecchia, W. Drozdowski, K. Brylew, W. Lachmanski, A. Bruno and C. Soci, X-ray Scintillation in Lead Halide Perovskite Crystals, *Sci. Rep.*, 2016, **6**, 37254.
 - 28 T. T. Kuo, C. M. Wu, H. H. Lu, I. Chan, K. Wang and K. C. Leou, Flexible x-ray imaging detector based on direct conversion in amorphous selenium, *J. Vac. Sci. Technol., A*, 2014, **32**(4), 041507.
 - 29 Y. W. Li, L. Meng, Y. Yang, G. Y. Xu, Z. R. Hong, Q. Chen, J. B. You, G. Li, Y. Yang and Y. F. Li, High-efficiency robust perovskite solar cells on ultrathin flexible substrates, *Nat. Commun.*, 2016, **7**, 10214.
 - 30 G. R. Bade, X. Shan, P. T. Hoang, J. Q. Li, T. Geske, L. Cai, Q. B. Pei, C. Wang and Z. B. Yu, Stretchable Light-Emitting Diodes with Organometal-Halide-Perovskite-Polymer Composite Emitters, *Adv. Mater.*, 2017, **29**(23), 1607053.
 - 31 S. G. R. Bade, J. Q. Li, X. Shan, Y. C. Ling, Y. Tian, T. Dilbeck, T. Besara, T. Geske, H. W. Gao, B. W. Ma, K. Hanson, T. Siegrist, C. Y. Xu and Z. B. Yu, Fully Printed Halide Perovskite Light-Emitting Diodes with Silver Nanowire Electrodes, *ACS Nano*, 2016, **10**(2), 1795–1801.
 - 32 M. R. Filip, S. Hillman, A. A. Haghighirad, H. J. Snaith and F. Giustino, Band Gaps of the Lead-Free Halide Double Perovskites Cs₂BiAgCl₆ and Cs₂BiAgBr₆ from Theory and Experiment, *J. Phys. Chem. Lett.*, 2016, **7**(13), 2579–2585.
 - 33 P. Zhang, J. X. Yang and S. H. Wei, Manipulation of cation combinations and configurations of halide double perovskites for solar cell absorbers, *J. Mater. Chem. A*, 2018, **6**(4), 1809–1815.
 - 34 M. R. Filip, X. L. Liu, A. Miglio, G. Hautier and F. Giustino, Phase Diagrams and Stability of Lead-Free Halide Double Perovskites Cs₂BB'X₆: B = Sb and Bi, B' = Cu, Ag, and Au, and X = Cl, Br, and I, *J. Phys. Chem. C*, 2018, **122**(1), 158–170.
 - 35 X. Li, M. I. Dar, C. Y. Yi, J. S. Luo, M. Tschumi, S. M. Zakeeruddin, M. K. Nazeeruddin, H. W. Han and M. Gratzel, Improved performance and stability of perovskite solar cells by crystal crosslinking with alkylphosphonic acid omega-ammonium chlorides, *Nat. Chem.*, 2015, **7**(9), 703–711.
 - 36 R. Kapadia, Z. B. Yu, H. H. H. Wang, M. Zheng, C. Battaglia, M. Hettick, D. Kiriya, K. Takei, P. Lobaccaro, J. W. Beeman, J. W. Ager, R. Maboudian, D. C. Chrzan and A. Javey, A direct thin-film path towards low-cost large-area III-V photovoltaics, *Sci. Rep.*, 2013, **3**, 2275.
 - 37 E. T. McClure, M. R. Ball, W. Windl and P. M. Woodward, Cs₂AgBiX₆ (X = Br, Cl): New Visible Light Absorbing, Lead-Free Halide Perovskite Semiconductors, *Chem. Mater.*, 2016, **28**(5), 1348–1354.
 - 38 L. T. Dou, Y. Yang, J. B. You, Z. R. Hong, W. H. Chang, G. Li and Y. Yang, Solution-processed hybrid perovskite photo-detectors with high detectivity, *Nat. Commun.*, 2014, **5**, 5404.
 - 39 Z. B. Yu, X. F. Niu, Z. T. Liu and Q. B. Pei, Intrinsically Stretchable Polymer Light Emitting Devices Using Carbon Nanotube-Polymer Composite Electrodes, *Adv. Mater.*, 2011, **23**, 3989–3994.
 - 40 Z. B. Yu, Q. W. Zhang, L. Li, Q. Chen, X. F. Niu, J. Liu and Q. B. Pei, Highly Flexible Silver Nanowire Electrodes for Shape-Memory Polymer Light-emitting Diodes, *Adv. Mater.*, 2011, **23**, 664–668.